nanomaterials

MDPI

Article

A Study of Inverted-Type Perovskite Solar Cells with Various Composition Ratios of $(FAPbI_3)_{1-x}(MAPbBr_3)_x$

Lung-Chien Chen *, Zong-Liang Tseng and Jun-Kai Huang

Department of Electro-Optical Engineering, National Taipei University of Technology, No. 1, Sec. 3, Chung-Hsiao E. Rd., Taipei 10608, Taiwan; tw78787788@yahoo.com.tw (Z.-L.T.); t103658032@ntut.org.tw (J.-K.H.)

* Correspondence: ocean@ntut.edu.tw; Tel.: +886-2-2772-2171

Academic Editor: Hao-chung Kuo

Received: 5 September 2016; Accepted: 10 October 2016; Published: 13 October 2016

Abstract: This work presents mixed $(FAPbI_3)_{1-x}(MAPbBr_3)_x$ perovskite films with various composition ratios, x (x = 0–1), which are formed using the spin coating method. The structural, optical, and electronic behaviors of the mixed $(FAPbI_3)_{1-x}(MAPbBr_3)_x$ perovskite films are discussed. A device with structure glass/indium tin oxide (ITO)/poly(3,4-ethylenedioxythiophene) polystyrene sulfonate (PEDOT:PSS)/mixed perovskite/C_{60}/BCP/Ag was fabricated. The mixed perovskite film was an active light-harvesting layer. PEDOT:PSS was a hole transporting layer between the ITO and perovskite. Both C_{60} and bathocuproine (BCP) were electron transporting layers. $MAPbBr_3$ was added to $FAPbI_3$ with a composition ratio of x = 0.2, stabilizing the perovskite phase, which exhibited a uniform and dense morphology. The optimal device exhibited band matching with C_{60}, resulting in a low series resistance (R_{sh}) and a high fill factor (FF). Therefore, the device with composition $(FAPbI_3)_{1-x}(MAPbBr_3)_x$ and x = 0.2 exhibited outstanding performance.

Keywords: $MAPbBr_3$; $FAPbI_3$; solar cells; perovskite

1. Introduction

Organometal halide perovskite solar cells have been intensively investigated owing to their high power conversion efficiency and fabrication in solution at low temperatures. Perovskite solar cells with an efficiency of over 20% have been fabricated [1–4]. The excellent performance of organometal halide perovskite solar cells has two causes: a small bandgap and a large exciton diffusion length. The low absorption bandgap (E_g of $CH_3NH_3PbI_3$ ($MAPbI_3$) ~1.5 eV) of organometal halide perovskite can harvest most wavelengths of incident sunlight. The long exciton diffusion length increases the thickness of active light-harvesting layers and ensures efficient carrier generation [5,6]. Moreover, the conventional structure of perovskite solar cells use TiO_2 for electron transport, but the TiO_2 needs to be processed using high temperatures (500–600 °C), and many applications are limited. Inverted-type perovskite solar cells have been developed for low-temperature process and low hysteresis [7].

Interestingly, the compositional engineering of perovskite materials has been extensively utilized to adjust their bandgap and structural properties for use in efficient perovskite solar cells. $CH_3NH_3PbI_{3-x}Br_x$ (x = 0.1–0.15), as an absorbing layer, has been reported to improve the open voltage of photovoltaic devices [8]. $CH_3NH_3PbI_{3-x}Cl_x$ has been used to increase the exciton diffusion length to improve device performance [9–12]. $HC(NH_2)_2PbI_3$ ($FAPbI_3$) [13–16] can reduce the optical bandgap (Eg ~1.48 eV), with an absorption edge of 840 nm, allowing photons to be absorbed over a broader solar spectrum. Accordingly, $FAPbI_3$ absorbs more light than $MAPbI_3$. Another advantage of $FAPbI_3$ is its thermal stability [17]. It can be processed at a higher temperature than can $MAPbI_3$. The typical annealing process temperature is approximately 130–170 °C. In particular, Jeon et al. explained that $(FAPbI_3)_{1-x}(MAPbBr_3)_x$ can provide a greater balance between electron transport and

the hole transport in cells, enabling highly efficient perovskite solar cells to be formed using a regular TiO_2 mesoscopic structure (>20%) [4]. However, the origin of their favorable performances and their fabrication process are not yet fully understood.

In this work, solution-processed $(FAPbI_3)_{1-x}(MAPbBr_3)_x$ perovskites were prepared on poly(3,4-ethylenedioxythiophene) polystyrene sulfonate (PEDOT:PSS)-coated indium tin oxide (ITO) substrates for use in inverted perovskite solar cells. The optical, structural, and surface properties of the $(FAPbI_3)_{1-x}(MAPbBr_3)_x$ perovskite films were studied as functions of the composition ratio (x = 0–1). The dependence of cell performance and the properties of the perovskite films is discussed.

2. Materials and Methods

In this work, a PEDOT:PSS (AI 4083) was spin-coated on a pre-cleaned ITO substrate at 5000 rpm for 30 s. Thereafter, the film was annealed at 120 °C for 10 min. The perovskite layer was deposited as in our previous investigation [18]. $HC(NH_2)_2I$ (FAI), PbI_2, CH_3NH_3Br (MABr), and $PbBr_2$ were dissolved in 1 mL of cosolvent, which comprised dimethyl sulfoxide (DMSO) and γ-butyrolactone (GBL) (volume ratio = 1:1), to form perovskite precursor solutions. The mole ratios of $FAPbI_3$ to $MAPbBr_3$ in the mixed perovskite varied from 0 to 1. The concentrations of each precursor were 1.2 M. For example, 0.96 mmol of $FAPbI_3$ and 0.24 mmol of $MAPbBr_3$ (i.e., 165 mg of FAI, 27 mg of MABr, 443 mg of PbI_2, and 88 mg of $PbBr_2$) were dissolved in the mixing solvent (1 mL) as a $(FAPbI_3)_{0.8}(MAPbBr_3)_{0.2}$ precursor solution. The perovskite precursor solutions were then coated onto the PEDOT:PSS/ITO substrate in two consecutive spin-coating steps, at 1000 rpm and 5000 rpm for 10 s and 20 s, respectively, in a glove box that was filled with highly pure nitrogen (>99.999%). The wet spinning film was quenched by dropping 50 μL of anhydrous toluene at 17 s. After spin coating, the film was annealed at 100 °C for 10 min. Subsequently, C_{60}, Bathocuproine (BCP), and a silver (Ag) electrode were deposited with thicknesses of 50, 5, and 100 nm, respectively, using a thermal evaporator. The sample was covered with a shadow mask to define an active area of 0.5 cm × 0.2 cm during C_{60}/BCP/Ag deposition. Figure 1a schematically depicts the complete structure.

Material and Device Measurement

The crystalline microstructures of the films were determined using a PAN analytical X'Pert Pro DY2840 X-ray diffractometer (PANalytical, Naerum, Denmark) with CuKα radiation (λ = 0.1541 nm). A field-emission scanning electron microscope (GeminiSEM, ZEISS, Oberkochen, Germany) was used to observe the surface morphology of the cells. Photoluminescence (PL) and absorption spectra were measured using a fluorescence spectrophotometer (Hitachi F-7000) and a UV/VIS/NIR spectrophotometer (Hitachi U-4100 spectrometers) (Hitachi High-Technologies Co., Tokyo, Japan), respectively. Current density–voltage (J-V) characteristics were measured using a Keithley 2420 programmable source meter (Keithley, Cleveland, OH, USA) under illumination by a 1000 W xenon lamp. The forward scan rate was 0.1 V/s.

3. Results and Discussion

Mixed perovskite film can be flexibly modified by changing the concentration ratio of the precursors [4,19]. The lowest unoccupied molecular orbitals (LUMOs) of $FAPbI_3$, $MAPbBr_3$, and C_{60} are −4.0, −3.6, and −3.9 eV, respectively [20,21]. The bandgap of the mixed $(FAPbI_3)_{1-x}(MAPbBr_3)_x$ film is between that of the $FAPbI_3$ film and that of the $MAPbBr_3$ film, from −4.0 to −3.6. To optimize the band matching with C_{60}, the composition ratio x of $FAPbI_3$ to $MAPbBr_3$ in the mixed $(FAPbI_3)_{1-x}(MAPbBr_3)_x$ perovskite is approximately 0.2 because the LUMO of the $(FAPbI_3)_{0.75}(MAPbBr_3)_{0.25}$ was determined by the interpolation to be −3.9, as shown in Figure 1b. Therefore, the device with the mixed $(FAPbI_3)_{0.75}(MAPbBr_3)_{0.25}$ perovskite film should have the lowest series resistance (R_{sh}).

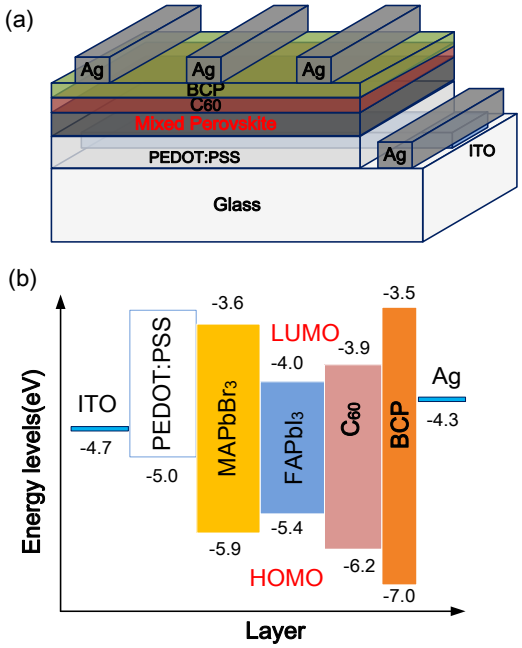

Figure 1. (**a**) Complete structure and (**b**) corresponding energy band diagram of the structure.

Figure 2 displays a high-resolution image of the cross-section of the obtained perovskite solar cell configuration, which clearly shows the presence of the layers ITO (200 nm), PEDOT:PSS (~50 nm), perovskite (~250 nm), C_{60} (~60 nm), and BCP (~10 nm). The grain size of the perovskite is approximately 200 nm, as presented in Figure 2. Numerous voids (indicated by red arrows) between grain boundaries were observed. These are characteristic of mixed $(FAPbI_3)_{1-x}(MAPbBr_3)_x$ perovskite films and may be attributed to the supersaturation nucleation and dynamic growth mechanism [22].

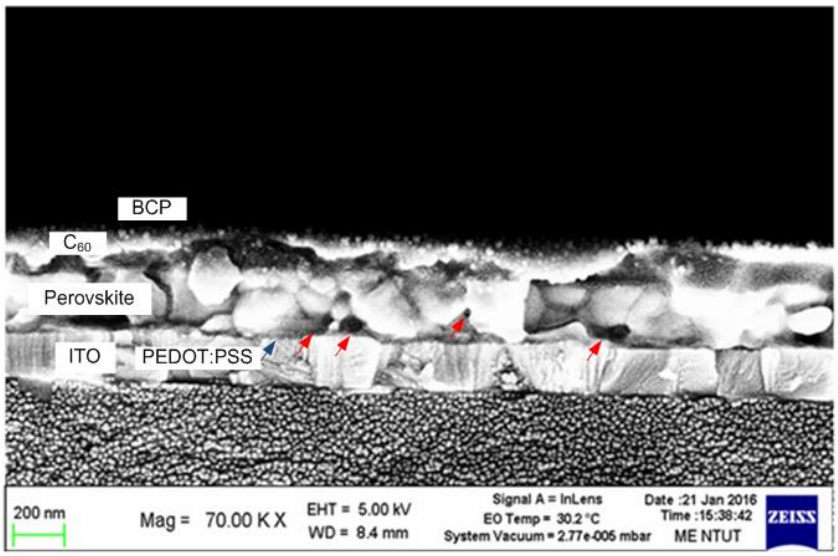

Figure 2. Field emission scanning electron microscope (FESEM) cross-sectional image of device structure.

Figure 3a shows the X-ray diffraction (XRD) patterns of $(FAPbI_3)_{1-x}(MAPbBr_3)_x$ perovskite films after thermal annealing at various temperatures. The spectrum of the $MAPbBr_3$ film includes three main diffraction peaks at 14.04°, which correspond to the δ-$FAPbI_3$, PbI_2, and α-$FAPbI_3$ phases, respectively. As the value of x in the $(FAPbI_3)_{1-x}(MAPbBr_3)_x$ perovskite films increases, the position of the α-$FAPbI_3$ phase peak shifts considerably to a high degree of diffraction, and the δ-FAPbI3 and

PbI_2 phase peaks disappear. The coexistence of the two $FAPbI_3$ and PbI_2 phases can be observed in the $(FAPbI_3)_{1-x}(MAPbBr_3)_x$ perovskite layers with $FAPbI_3$. The spectrum of the $MAPbBr_3$ film includes one diffraction peak at 15.03°, which corresponds to the (100) phase. As presented in Figure 3b, the peak position increases almost linearly with x, revealing that the crystalline $FAPbI_3$ and $MAPbBr_3$ are homogeneous.

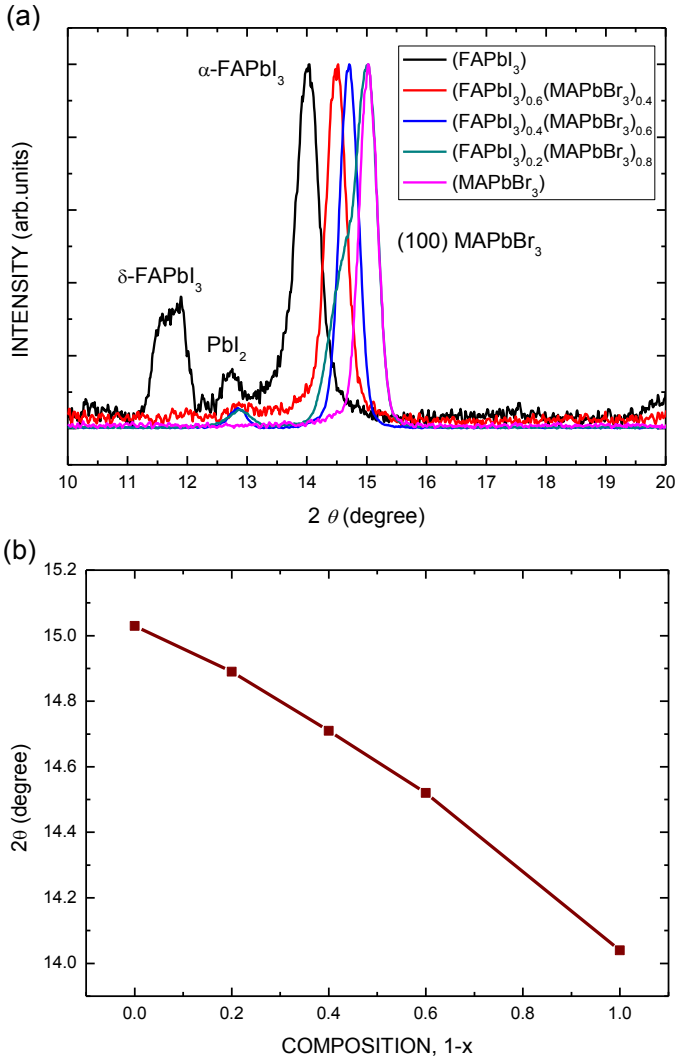

Figure 3. (**a**) X-ray diffraction (XRD) patterns of $(FAPbI_3)_{1-x}(MAPbBr_3)_x$ perovskite films with various compositions; (**b**) Relationship between degree of diffraction and composition of $(FAPbI_3)_{1-x}(MAPbBr_3)_x$.

Figure 4a presents the room-temperature PL spectra of $(FAPbI_3)_{1-x}(MAPbBr_3)_x$ films with various composition ratios that were deposited on glass substrates. The PL peak shifts nonlinearly from 804 to 533 nm as the composition ratio x is increased from 0 to 1, as displayed in Figure 4a. The bandgaps of $MAPbBr_3$ and $FAPbI_3$ are approximately 2.3 and 1.5 eV, respectively, and correspond to wavelengths of around 540 and 820 nm, respectively. Therefore, bandgap values and PL results match. The bandgap of the mixed $(FAPbI_3)_{1-x}(MAPbBr_3)_x$ perovskite films is calculated from the PL spectra, as shown in Figure 4b. The bandgap over the entire range of the $(FAPbI_3)_{1-x}(MAPbBr_3)_x$ perovskite films can be estimated from the PL spectra. Fitting the PL spectra at room temperature yields the following expression for the bandgap, Eg:

$$\mathrm{Eg}(x) = 1.5 + 0.2x^3 + 0.58x^6. \quad (1)$$

The expression is a sixth-order polynomial, rather than the traditional second-order polynomial for compound semiconductors, revealing that the bandgap of the mixed $(FAPbI_3)_{1-x}(MAPbBr_3)_x$ perovskite films is extremely sensitive to the composition of the mixed $(FAPbI_3)_{1-x}(MAPbBr_3)_x$ perovskite films when the concentration of the $FAPbI_3$ is low.

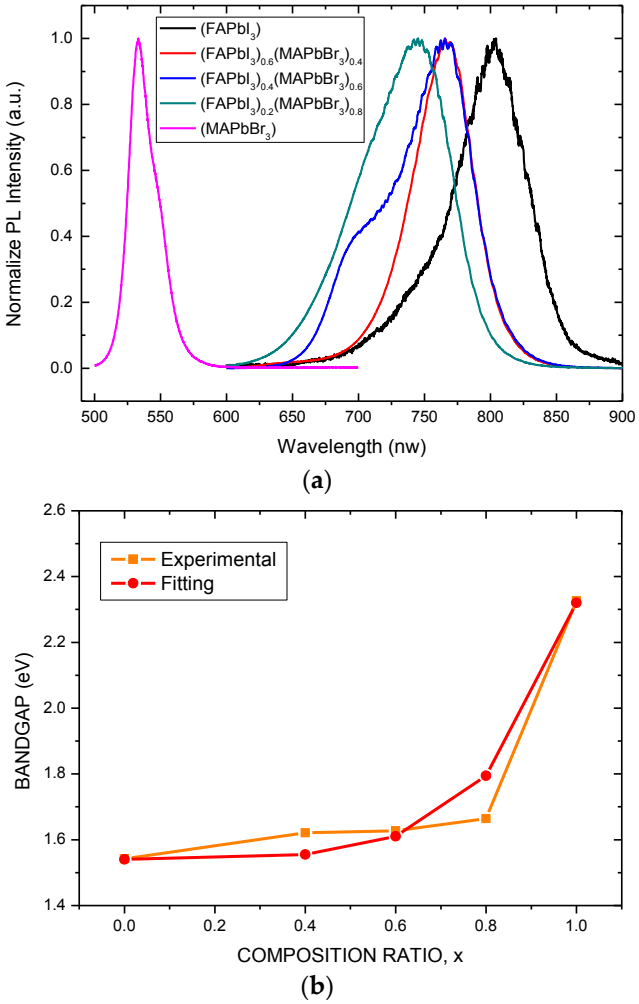

Figure 4. (**a**) Photoluminescence (PL) spectra of mixed $(FAPbI_3)_{1-x}(MAPbBr_3)_x$ perovskite films with various values of x. (**b**) Bandgap of mixed $(FAPbI_3)_{1-x}(MAPbBr_3)_x$ perovskite films, estimated from PL spectra.

Figure 5 plots the current density as a function of the voltage (J-V) of solar cells that are based on $(FAPbI_3)_{1-x}(MAPbBr_3)_x$ films with various composition ratios. Table 1 presents the power conversion efficiency (Eff), short-circuit current density (J_{sc}), open-circuit voltage (V_{oc}), and fill factor (FF) of the $(FAPbI_3)_{1-x}(MAPbBr_3)_x$ solar cells. The bandgap of the $(FAPbI_3)_{1-x}(MAPbBr_3)_x$ film is reduced as the proportion of $(MAPbBr_3)$ in the $(FAPbI_3)_{1-x}(MAPbBr_3)_x$ films increases. The power conversion efficiency increases with x in the $(FAPbI_3)_{1-x}(MAPbBr_3)_x$ films because J_{sc} increases with the strength of absorption and the amount of α-$FAPbI_3$ formed. However, the power conversion efficiency decreases as more $MAPbBr_3$ is formed owing to a reduction in the photocurrent and series resistance (R_{sh}). The optimal device, with a $(FAPbI_3)_{0.8}(MAPbBr_3)_{0.2}$ perovskite film, exhibited outstanding performance, where J_{sc} = 20.6 mA/cm^2, V_{oc} = 0.88 V, FF = 65.9%, and Eff = 12.0%. $MAPbBr_3$ was added to $FAPbI_3$ where x = 0.2 to stabilize the perovskite phase with a uniform and dense morphology [4]. Therefore, the device with the $(FAPbI_3)_{0.8}(MAPbBr_3)_{0.2}$ perovskite film exhibited the lowest series resistance (R_{sh}), the best FF, and therefore the best performance.

The bandgap of the $(FAPbI_3)_{1-x}(MAPbBr_3)_x$ film is reduced as the amount of $MAPbBr_3$ in the $(FAPbI_3)_{1-x}(MAPbBr_3)_x$ film increases. Therefore, by increasing the composition ratio x, the $(FAPbI_3)_{1-x}(MAPbBr_3)_x$ film increases the LUMO of the $(FAPbI_3)_{1-x}(MAPbBr_3)_x$ film to match that of the C_{60} layer and increases the energy barrier to the transportation of electrons, resulting in a low FF. The value of V_{oc} is positively correlated with the difference between the highest occupied molecular orbital (HOMO) of the $(FAPbI_3)_{1-x}(MAPbBr_3)_x$ film and the LUMO of the C_{60} layer (Figure 1b) [23]. Therefore, V_{oc} is determined by the increase in the HOMO level of the $(MAPbBr_3)_x(FAPbI_3)_{1-x}$ film. The bandgap of the $(FAPbI_3)_{1-x}(MAPbBr_3)_x$ film increases with x, increasing V_{oc}. Additionally, the LUMO level of the $(MAPbBr_3)_x(FAPbI_3)_{1-x}$ film is lower than that of C_{60}, so an energy barrier is formed, lowering FF. Additionally, the photo-generated current density declines as the proportion of $MAPbBr_3$ in the $(FAPbI_3)_{1-x}(MAPbBr_3)_x$ films increases because the absorption range is reduced.

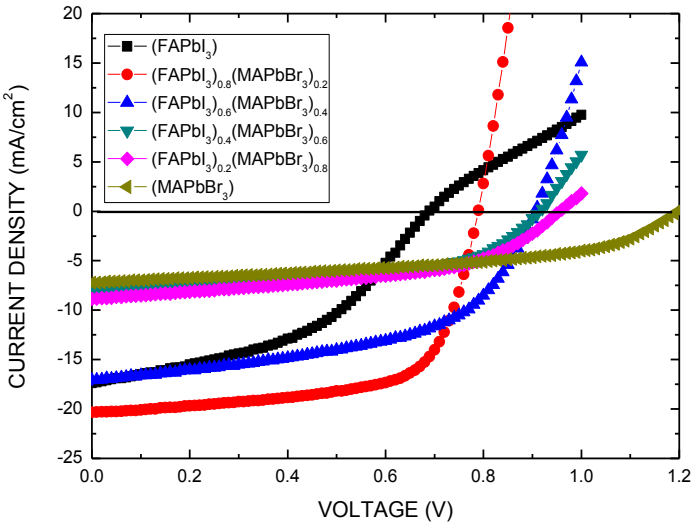

Figure 5. J-V curves of perovskite solar cell (Ag/BCP/C_{60}/$(FAPbI_3)_{1-x}(MAPbBr_3)_x$/PEDOT:PSS/ITO) obtained under standard 1 sun air mass (AM) 1.5 simulated solar irradiation.

Table 1. Parameters of solar cells based on perovskite $(FAPbI_3)_{1-x}(MAPbBr_3)_x$ film with various composition ratios.

$(FAPbI_3)_{1-x}(MAPbBr_3)_x$	V_{oc} (V)	J_{sc} (mA/cm^2)	FF (%)	Eff (%)	R_{sh} (Ω)
$(FAPbI_3)$	0.60	17.3	44.0	5.68	20.3
$(FAPbI_3)_{0.8}(MAPbBr_3)_{0.2}$	0.88	20.6	65.9	12.0	4.6
$(FAPbI_3)_{0.6}(MAPbBr_3)_{0.4}$	0.90	17.63	52.9	9.41	8.5
$(FAPbI_3)_{0.4}(MAPbBr_3)_{0.6}$	0.90	11.01	51.4	5.51	19.8
$(FAPbI_3)_{0.2}(MAPbBr_3)_{0.8}$	0.95	8.86	49.4	4.18	21.2
$(MAPbBr_3)_1$	1.2	7.23	47.7	4.19	30.6

4. Conclusions

In summary, this work presents mixed $(FAPbI_3)_{1-x}(MAPbBr_3)_x$ perovskite films with various composition ratios (x = 0 to 1), formed using the spin coating method. The bandgap over the entire range of the $(FAPbI_3)_{1-x}(MAPbBr_3)_x$ perovskite films can be estimated from the PL spectra. Fitting the PL spectra yields a sixth-order polynomial for the bandgap of the mixed $(FAPbI_3)_{1-x}(MAPbBr_3)_x$ perovskite films. This result reveals that the bandgap of the mixed $(FAPbI_3)_{1-x}(MAPbBr_3)_x$ perovskite films is extremely sensitive to the composition of the mixed $(FAPbI_3)_{1-x}(MAPbBr_3)_x$ perovskite films when the concentration of the $FAPbI_3$ is low. The optimal device uses $(FAPbI_3)_{1-x}(MAPbBr_3)_x$ with x = 0.2 and exhibited outstanding performance, where short-circuit current density J_{sc} = 20.6 mA/cm^2, open-circuit voltage V_{oc} = 0.88 V, fill factor FF = 65.9%, and power conversion efficiency Eff = 12.0%,

perhaps because the addition of $MAPbBr_3$ to $FAPbI_3$ where $x = 0.2$ stabilized the perovskite phase with a uniform and dense morphology. The optimum device exhibits band matching with C_{60}, resulting in a low series resistance (R_{sh}) and high FF.

Acknowledgments: Financial support of this paper was provided by the Ministry of Science and Technology of the Republic of China under Contract no. MOST 105-2221-E-027-055.

Author Contributions: Lung-Chien Chen wrote the paper, designed the experiments, and analyzed the data. Zong-Liang Tseng and Jun-Kai Huang prepared the samples and performed all the measurements. All authors read and approved the final manuscript.

Conflicts of Interest: The authors declare no conflicts of interest.

References

1. Yang, W.S.; Noh, J.H.; Jeon, N.J.; Kim, Y.C.; Ryu, S.; Seo, J.; Seok, S.I. High-performance photovoltaic perovskite layers fabricated through intramolecular exchange. *Science* **2015**, *348*, 1234–1237. [CrossRef] [PubMed]
2. Liu, M.; Johnston, M.B.; Snaith, H.J. Efficient planar heterojunction perovskite solar cells by vapour deposition. *Nature* **2013**, *501*, 395–398. [CrossRef] [PubMed]
3. Im, J.-H.; Jang, I.-H.; Pellet, N.; Grätzel, M.; Park, N.-G. Growth of $CH_3NH_3PbI_3$ cuboids with controlled size for high-efficiency perovskite solar cells. *Nat. Nano* **2014**, *9*, 927–932. [CrossRef] [PubMed]
4. Jeon, N.J.; Noh, J.H.; Yang, W.S.; Kim, Y.C.; Ryu, S.; Seo, J.; Seok, S.I. Compositional engineering of perovskite materials for high-performance solar cells. *Nature* **2015**, *517*, 476–480. [CrossRef] [PubMed]
5. Xing, G.; Mathews, N.; Sun, S.; Lim, S.S.; Lam, Y.M.; Grätzel, M.; Mhaisalkar, S.; Sum, T.C. Long-Range Balanced Electron- and Hole-Transport Lengths in Organic-Inorganic $CH_3NH_3PbI_3$. *Science* **2013**, *342*, 344–347. [CrossRef] [PubMed]
6. Stranks, S.D.; Eperon, G.E.; Grancini, G.; Menelaou, C.; Alcocer, M.J.P.; Leijtens, T.; Herz, L.M.; Petrozza, A.; Snaith, H.J. Electron-Hole Diffusion Lengths Exceeding 1 Micrometer in an Organometal Trihalide Perovskite Absorber. *Science* **2013**, *342*, 341–344. [CrossRef] [PubMed]
7. Chen, L.-C.; Wu, J.-R.; Tseng, Z.-L.; Chen, C.-C.; Chang, S.-H.; Huang, J.-K.; Lee, K.-L.; Cheng, H.-M. Annealing Effect on $(FAPbI_3)_{1-x}(MAPbBr_3)_x$ Perovskite Films in Inverted-Type Perovskite Solar Cells. *Materials* **2016**, *9*, 747. [CrossRef]
8. Jeon, N.J.; Noh, J.H.; Kim, Y.C.; Yang, W.S.; Ryu, S.; Seok, S.I. Solvent engineering for high-performance inorganic–organic hybrid perovskite solar cells. *Nat. Mater.* **2014**, *13*, 897–903. [CrossRef] [PubMed]
9. Shi, Y.; Xing, Y.; Li, Y.; Dong, Q.; Wang, K.; Du, Y.; Bai, X.; Wang, S.; Chen, Z.; Ma, T. $CH_3NH_3PbI_3$ and $CH3NH_3PbI_{3-x}Cl_x$ in Planar or Mesoporous Perovskite Solar Cells: Comprehensive Insight into the Dependence of Performance on Architecture. *J. Phys. Chem. C* **2015**, *119*, 15868–15873. [CrossRef]
10. Cao, C.; Zhang, C.; Yang, J.; Sun, J.; Pang, S.; Wu, H.; Wu, R.; Gao, Y.; Liu, C. Iodine and Chlorine Element Evolution in $CH_3NH_3PbI_{3-x}Cl_x$ Thin Films for Highly Efficient Planar Heterojunction Perovskite Solar Cells. *Chem. Mater.* **2016**, *28*, 2742–2749. [CrossRef]
11. Liu, D.; Wu, L.; Li, C.; Ren, S.; Zhang, J.; Li, W.; Feng, L. Controlling $CH_3NH_3PbI_{3-x}Cl_x$ Film Morphology with Two-Step Annealing Method for Efficient Hybrid Perovskite Solar Cells. *ACS Appl. Mater. Inter.* **2015**, *7*, 16330–16337. [CrossRef] [PubMed]
12. Chen, Q.; Zhou, H.; Fang, Y.; Stieg, A.Z.; Song, T.-B.; Wang, H.-H.; Xu, X.; Liu, Y.; Lu, S.; You, J.; et al. The optoelectronic role of chlorine in $CH_3NH_3PbI_3$(Cl)-based perovskite solar cells. *Nat. Commun.* **2015**, *6*. [CrossRef] [PubMed]
13. Wang, Z.; Zhou, Y.; Pang, S.; Xiao, Z.; Zhang, J.; Chai, W.; Xu, H.; Liu, Z.; Padture, N.P.; Cui, G. Additive-Modulated Evolution of $HC(NH_2)_2PbI_3$ Black Polymorph for Mesoscopic Perovskite Solar Cells. *Chem. Mater.* **2015**, *27*, 7149–7155. [CrossRef]
14. Zhou, Y.; Kwun, J.; Garces, H.F.; Pang, S.; Padture, N.P. Observation of phase-retention behavior of the $HC(NH_2)_2PbI_3$ black perovskite polymorph upon mesoporous TiO_2 scaffolds. *Chem. Commun.* **2016**, *52*, 7273–7275. [CrossRef] [PubMed]
15. Song, J.; Hu, W.; Wang, X.-F.; Chen, G.; Tian, W.; Miyasaka, T. $HC(NH_2)_2PbI_3$ as a thermally stable absorber for efficient ZnO-based perovskite solar cells. *J. Mater. Chem. A* **2016**, *4*, 8435–8443. [CrossRef]

16. Lee, J.-W.; Seol, D.-J.; Cho, A.-N.; Park, N.-G. High-Efficiency Perovskite Solar Cells Based on the Black Polymorph of $HC(NH_2)_2PbI_3$. *Adv. Mater.* **2014**, *26*, 4991–4998. [CrossRef] [PubMed]
17. Zhou, Y.; Zhu, K. Perovskite Solar Cells Shine in the "Valley of the Sun". *ACS Energy Lett.* **2016**, *1*, 64–67. [CrossRef]
18. Chen, L.-C.; Chen, C.-C.; Chen, J.-C.; Wu, C.-G. Annealing effects on high-performance $CH_3NH_3PbI_3$ perovskite solar cells prepared by solution-process. *Solar Energy* **2015**, *122*, 1047–1051. [CrossRef]
19. Kulkarni, S.A.; Baikie, T.; Boix, P.P.; Yantara, N.; Mathews, N.; Mhaisalkar, S. Band-gap tuning of lead halide perovskites using a sequential deposition process. *J. Mater. Chem. A* **2014**, *2*, 9221–9225. [CrossRef]
20. Aharon, S.; Dymshits, A.; Rotem, A.; Etgar, L. Temperature dependence of hole conductor free formamidinium lead iodide perovskite based solar cells. *J. Mater. Chem. A* **2015**, *3*, 9171–9178. [CrossRef]
21. Schueppel, R.; Schmidt, K.; Uhrich, C.; Schulze, K.; Wynands, D.; Brédas, J.L.; Brier, E.; Reinold, E.; Bu, H.B.; Baeuerle, P.; et al. Optimizing organic photovoltaics using tailored heterojunctions: A photoinduced absorption study of oligothiophenes with low band gaps. *Phys. Rev. B* **2008**, *77*, 085311. [CrossRef]
22. Zhou, Y.; Game, O.S.; Pang, S.; Padture, N.P. Microstructures of Organometal Trihalide Perovskites for Solar Cells: Their Evolution from Solutions and Characterization. *J. Phys. Chem. Lett.* **2015**, *6*, 4827–4839. [CrossRef] [PubMed]
23. Jeng, J.Y.; Chiang, Y.F.; Lee, M.H.; Peng, S.R.; Guo, T.F.; Chen, P.; Wen, T.C. $CH_3NH_3PbI_3$ perovskite/fullerene planar-heterojunction hybrid solar cells. *Adv. Mater.* **2013**, *25*, 3727–3732. [CrossRef] [PubMed]